scientific reports

Check for updates

OPEN

One-step preparation of RGO/Fe_3O_4–$FeVO_4$ nanocomposites as highly effective photocatalysts under natural sunlight illumination

Qana A. Alsulami[1]✉, A. Rajeh[2], Mohammed A. Mannaa[3], Soha M. Albukhari[1] & Doaa F. Baamer[1]

The study used a one-step hydrothermal method to prepare Fe_3O_4–$FeVO_4$ and xRGO/Fe_3O_4–$FeVO_4$ nanocomposites. XRD, TEM, EDS, XPS, DRS, and PL techniques were used to examine the structurally and morphologically properties of the prepared samples. The XRD results appeared that the Fe_3O_4–$FeVO_4$ has a triclinic crystal structure. Under hydrothermal treatment, (GO) was effectively reduced to (RGO) as illustrated by XRD and XPS results. UV–Vis analysis revealed that the addition of RGO enhanced the absorption in the visible region and narrowed the band gap energy. The photoactivities of the prepared samples were evaluated by degrading methylene blue (MB), phenol and brilliant green under sunlight illumination. As indicated by all the nanocomposites, photocatalytic activity was higher than the pure Fe_3O_4–$FeVO_4$ photocatalyst, and the highest photodegradation efficiency of MB and phenol was shown by the 10%RGO/Fe_3O_4–$FeVO_4$. In addition, the study examined the mineralization (TOC), photodegradation process, and photocatalytic reaction kinetics of MB and phenol.

The world of today is seeking state-of-the-art technologies to deal with the major challenges of the environment pollutions[1–3]. The fast industry expansion and development, water becomes contaminated, carrying significant concentrations of hazardous and dangerous contaminants such as dyes, inks, pesticides, and so on[4–6]. Almost 10–15% of dyes are released in the environment during the dying process, contaminating sewage water[7]. Many attempts were taken in order to use new and various light sources and nanomaterials for removal of organic pollutants by photodegradation method[7–10]. Different approaches like doping and compositing used to enhance the structural properties and photodegradation efficiency of the prepared nanomaterials. Various modified metal oxide such as, Vanadium doped $CaTiO_3$[11], Rh doped $SrTiO_3$[12], Rhodium doping barium titanate[13], Graphene Wrapped SrTiO3 Nanocomposite[14], … etc. have been prepared by different approaches and applied as efficient photocatalysts.

Meta-vanadates, which are characterized as cohesive materials' class and have prospective uses in various fields, are one of former mentioned materials[1,15]. In addition, because of its various stable oxidizing states (+2 to +5), vanadium interacts with numerous components. However, $FeVO_4$ gave low photocatalytic activity, low optical absorption and poor transport of photogenerated charges which limited its applications[7,16]. Many novel composites are created as a result of this combining procedure. Fe_3O_4–$FeVO_4$ in particular stands out for its broad range of beneficial properties[17]. It has been investigated for distinctive applications due to its advantageous properties, including ease of preparation, low cost, environmental friendliness, and small band gap[17,18]. The present investigation could not be carried out without Fe_3O_4–$FeVO_4$ feature of small band gap (2.7–2.03 eV)[1,19]. Furthermore, Fe_3O_4–$FeVO_4$ has the necessary conductivity and energy levels to format nanocomposite catalysts[15,17]. In addition, it was revealed that Fe_3O_4–$FeVO_4$ catalysts were effective applied in the treatment of various organic contaminants present in water over a wider pH range. A varying of methods were applied for water purification[20]. The photocatalysis method does not entail an issue of waste disposal. Furthermore, a lot of composite materials were prepared with graphene and the resultant composites displayed different advantages and applied in various sectors. For example, various composites including $FeVO_4{\cdot}xH_2O$/Graphene[21], ZnO/$FeVO_4$[22], $FeVO_4$/$Bi_7O_9I_3$[23] rGO-$FeVO_4$[15], RGO–$ZnWO_4$–Fe_3O_4[24], N-doped RGO-$FeWO_4$/Fe_3O_4[25] $BaWO_4$/NRGO–g-C_3N_4[26], and RGO–$ZnWO_4$[14] have recently been prepared and applied in different sectors.

[1]Chemistry Department, Faculty of Science, King Abdulaziz University, Jeddah, Saudi Arabia. [2]Physics Department, Faculty of Science, Amran University, Amran, Yemen. [3]Chemistry Department, Faculty of Science, Amran University, Amran, Yemen. ✉email: qalselami@kau.edu.sa

In addition, RGO-based ortho-vanadates were applied as useful material for water[20]. In this research, Fe_3O_4–$FeVO_4$ and xRGO/Fe_3O_4–$FeVO_4$ with various RGO quantities were prepared. The hydrothermal technique was used to efficiently decrease GO to RGO. The study was investigated the influence of RGO quantity on the structural characteristics and photocatalytic effectiveness of Fe_3O_4–$FeVO_4$. The photocatalytic activities of the prepared samples were examined by the photodegradation of MB, phenol and brilliant green (BG) solution under natural sunlight illumination. The xRGO/Fe_3O_4–$FeVO_4$ demonstrated excellent charges separation, stability, reusability, and photocatalytic activity, indicating that it is a potential material for a variety of environmental applications.

Experimental

Preparation of GO. Graphene oxide (GO) was prepared as described in our previous literature[27].

Preparation of Fe_3O_4–$FeVO_4$ and xRGO/Fe_3O_4–$FeVO_4$ nanocomposites. The hydrothermal technique was used to produce Fe_3O_4–$FeVO_4$ and xRGO/Fe_3O_4–$FeVO_4$ nanocomposites. According to this technique, 3 mmol of Fe $(NO_3)_3{\cdot}9H_2O$ was dissolved in 10 ml of HNO_3 solution with the concentration of 1 mol/L. 3 mmol NH_4VO_3 (Sigma-Aldrich) was dissolved in 10 ml of deionized water and kept at ultrasonic bath @50 °C for 30 min. After that, the solution of Fe $(NO_3)_3$ was added into NH_4VO_3 solution under vigorous agitation for 1 h. A certain quantity of the prepared GO was suspended in 20 ml of ethanol solution (2:1) under vigorously stirring and ultrasonicated for 1 h and then added to the mixture under magnetic agitation for 2 h. Finally, the resultant mixture was transferred to an autoclave with 50 ml volume and kept at 200 °C for 2 h. In comparison, a similar technique was used to produce pure Fe_3O_4–$FeVO_4$ without RGO.

Characterization methods. Crystal structure of the prepared samples was characterized by X-ray diffraction (XRD, Bruker-D8-AXS diffractometer, Germany) with Cu-Kα radiation at a setting of 40 kV and 150 mA. The images were captured using a transmission electron microscope (TEM) with a Jeol JEM-1230 apparatus operating at 120 kV. With the same EDAX detector, an energy-dispersive X-ray (EDx) study was performed (SEM, Hitachi S-4200). The chemical compositions (Axis Ultra DLD, Kratos) were performed using X-ray photoelectron spectroscopy (XPS) with a 325 nm excitation wavelength. At room temperature, UV–visible absorption studies were conducted by the UV−Vis 2450 (Shimadzu) spectrophotometer to record diffuse reflectance spectra (DRS). The photoluminescence (PL) spectra were carried out with a fluorescent spectrophotometer (HORIBA-Jobin-Yvon).

Photocatalytic activity study. *Photodegradation studies.* The photocatalytic activity of the produced catalysts was assessed for MB, phenol and BG photodegradation. Natural sunshine provided irradiation, and the reactor was encased in a water-cooling system. The solution was transported to the photoreactor after 0.05 g of sample powder was added to 50 ml of pollutant (Co = 10 MB/L). The degradation of MB, phenol and BG in solar light was performed on sunny days between 11.00 a.m. and 2.00 p.m. with a maximum temperature of 35 °C. The intensity solar light was measured every 30 min over LT Lutron LX-10/A digital Lux meter and the average light intensity was nearly constant during the experiments. The mixture was first agitated in the dark for 30 min to achieve the adsorption–desorption equilibrium. The mixture was then stirred on a magnetically under direct sunshine lighting. The degradation of MB, phenol and BG was calculated using the Eq. (1)[28], and the change in pollutant concentrations was measured using a Shimadzu, MPC-2200 UV–Vis spectrophotometer.

$$D\% = \left(\frac{C_o - C_t}{C_o}\right) \times 100\% \quad (1)$$

where C_o and C_t represent the concentrations dyes before and after irradiation, respectively (t). The reactive radicals that might be formed in photocatalytic processes were also investigated employing several scavengers at concentrations of 1 mM, including benzoquinone (BQ), isopropanol (IPA), and Na_2EDTA as $^{\cdot}O_2^-$, $^{\cdot}OH$, and h^+ scavengers, respectively[29–31]. The total organic carbon (TOC) was measured using a Shimadzu 5000 TOC Analyzer which applied to investigate the mineralization of MB, phenol and BG. After photodegradation, the %TOC of MB, phenol and BG was estimated using the following equation:

$$\%TOC = \left(\frac{TOC_{Initial} - TOC_{Final}}{TOC_{Initial}}\right) \times 100 \quad (2)$$

Results and discussion

XRD analysis. The XRD patterns of Fe_3O_4–$FeVO_4$ and xRGO/Fe_3O_4–$FeVO_4$ nanocomposites are displayed in Fig. 1. The diffraction peaks of Fe_3O_4–$FeVO_4$ demonstrates that the sample have a triclinic phase (JCPDS card No. #71–1592)[3,19,32,33]. Further, another diffraction peaks appeared at 18.51°, 30.24°, 35.61° and 73.91° matched very well with the Fe_3O_4 structure (JCPDS No. 19-0629)[34].

The XRD patterns of xRGO/Fe_3O_4–$FeVO_4$ showed similar peaks as of Fe_3O_4–$FeVO_4$. Moreover, the sample with 15 wt.% of RGO displayed a small peak appeared at $2\theta = 26.05°$ indicating the existence of RGO[21,35]. As seen in Fig. 1S displays positional shift of the peaks after the addition of RGO. This resulted from effect the introduction of RGO which led to changes in the lattice parameters of Fe_3O_4–$FeVO_4$ (d-spacing changed from 3.17 to 3.19 Å at $2\theta = 27.9°$). In addition, Fig. 1 illustrates that the intensity of characteristic peaks increased with the percentage of RGO increased.

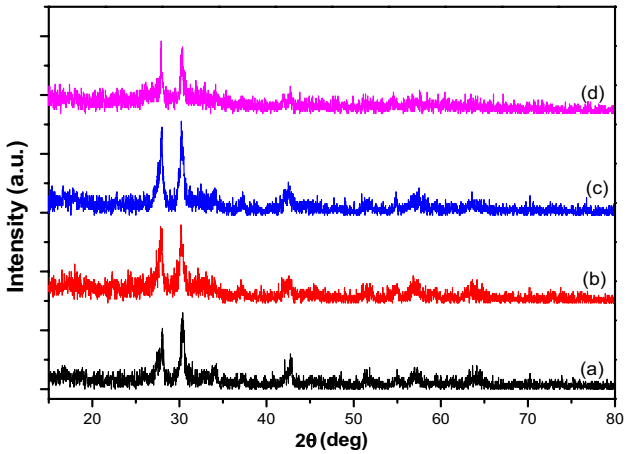

Figure 1. XRD patterns of (**a**) Fe_3O_4–$FeVO_4$ and (**b**) 5%, (**c**) 10%, (**d**) 15%RGO/Fe_3O_4–$FeVO_4$ nanocomposites.

Sample name	Crystallite size D (nm)	Band gap energy (eV)
Fe_3O_4–$FeVO_4$	72.9	2.07
5%RGO/Fe_3O_4–$FeVO_4$	79.6	2.04
10%RGO/Fe_3O_4–$FeVO_4$	88.1	1.9
15%RGO/Fe_3O_4–$FeVO_4$	85.8	1.98

Table 1. Crystallite size and BG energy of the prepared photocatalysts.

The crystal size of the prepared samples was calculated according to the Scherrer's equation[36,37]. Table 1 illustrates that the crystals size of xRGO/Fe_3O_4–$FeVO_4$ increased with the percentage of RGO increased compared to pure Fe_3O_4–$FeVO_4$ indicating the existence of RGO enhanced the crystals growth of Fe_3O_4–$FeVO_4$.

TEM and EDX analysis. The morphology and size of Fe_3O_4–$FeVO_4$ and xRGO/Fe_3O_4–$FeVO_4$ were characterized by TEM as depicted in Fig. 2. Figure 2a, b reveals that the Fe_3O_4–$FeVO_4$ have nanorod and spherical particles structures. The particles with nanorod structure indicate to the structure of Fe_3O_4–$FeVO_4$ while the spherical particles attribute to the Fe_3O_4. On the other hand, the particles with nanorods structure showed average size ~ 138 nm and ~ 20 nm in length and diameter while the spherical particles is 13.8 nm. Figure 2c illustrates the influence of the addition of reduced graphene oxide on the structure of Fe_3O_4–$FeVO_4$. TEM images of 10%Fe_3O_4–$FeVO_4$ (Fig. 2c) displays that the particles still have the nanorods shape. The HR-TEM images of Fe_3O_4–$FeVO_4$ and 10%RGO/Fe_3O_4–$FeVO_4$ are shown in Fig. 2c, e and displays that the d-spacing are 0.30, 0.32 and 0.33 nm where 0.30 nm approach to the (220) lattice plane of Fe_3O_4 (peak at $2\Theta = 30.24°$) while 0.32 nm belong to (1–12) plane of $FeVO_4$ ($2\Theta = 27.9°$). The increasing in the lattice spacing from 0.30 of Fe_3O_4–$FeVO_4$ to 0.32 nm of 10%RGO/Fe_3O_4–$FeVO_4$ resulted from effect the introduction of RGO as described in the XRD. In addition, Fig. 2e also reveals the formation of heterojunction interface between $FeVO_4$ and Fe_3O_4 on the RGO surface.

Figure 3 shows the EDX spectra of Fe_3O_4–$FeVO_4$ and xRGO/Fe_3O_4–$FeVO_4$. Figure 3a displays that the Fe_3O_4–$FeVO_4$ have Fe, V, C and O and no another impurities were detected. In addition, the 10%RGO/Fe_3O_4–$FeVO_4$ nanocomposites (Fig. 3b) showed the similar elements as Fe_3O_4–$FeVO_4$ and C which attributes to RGO in the sample. Also, Table 1S illustrates the weight percent of elements in the 10%RGO/Fe_3O_4–$FeVO_4$ which confirmed the successful preparation of the desired nanocomposites.

XPS studies. Figure 4 displays the XPS results of Fe_3O_4–$FeVO_4$ and 10%RGO/Fe_3O_4–$FeVO_4$. The XPS spectrum of Fe_3O_4–$FeVO_4$ in Fig. 4a presents peaks corresponding to Fe 2*p*, V 2*p*, and O 1*s* and the spectrum of 10%RGO/Fe_3O_4–$FeVO_4$ showed the same peaks as Fe_3O_4–$FeVO_4$ and C 1*s* in agreement with EDX results (Fig. 3).

The high-resolution spectra of Fe 2*p*, V 2*p*, O1*s* and C 1*s* are illustrated in Fig. 4b–d. As seen in Fig. 4b, Fe_3O_4–$FeVO_4$ displayed main binding energies appeared at 711.23 eV and 725.12 eV belongs to Fe $2p_{3/2}$ and Fe $2p_{1/2}$ respectively. Also, the satellite peak appeared at 717.45 eV assigned to Fe^{3+} in the sample[1,21,38]. Another peaks observed at 713.33 and 726.86 eV accompanied with its satellite appeared at 720.62 and 733.21 eV which confirmed the presence of Fe^{2+}[21]. Comparing with Fe_3O_4–$FeVO_4$, 10%RGO/Fe_3O_4–$FeVO_4$ displayed the same main binding energies as shown in Fig. 4b. Also, the intensity peaks of 10%RGO/Fe_3O_4–$FeVO_4$ are higher than that of Fe_3O_4–$FeVO_4$. Figure 4c shows the high-resolution spectrum of Fe_3O_4–$FeVO_4$. In this spectrum, six peaks were observed at 516.66, 516.83, 517.22, 523.14, 523.65 and 524.75 eV belong to V $2p_{3/2}$ and V $2p_{1/2}$ peaks. The positions of these peaks donating the existence of V^{4+} and V^{5+} of V[16,32,39]. New peaks located at 518.13 eV were

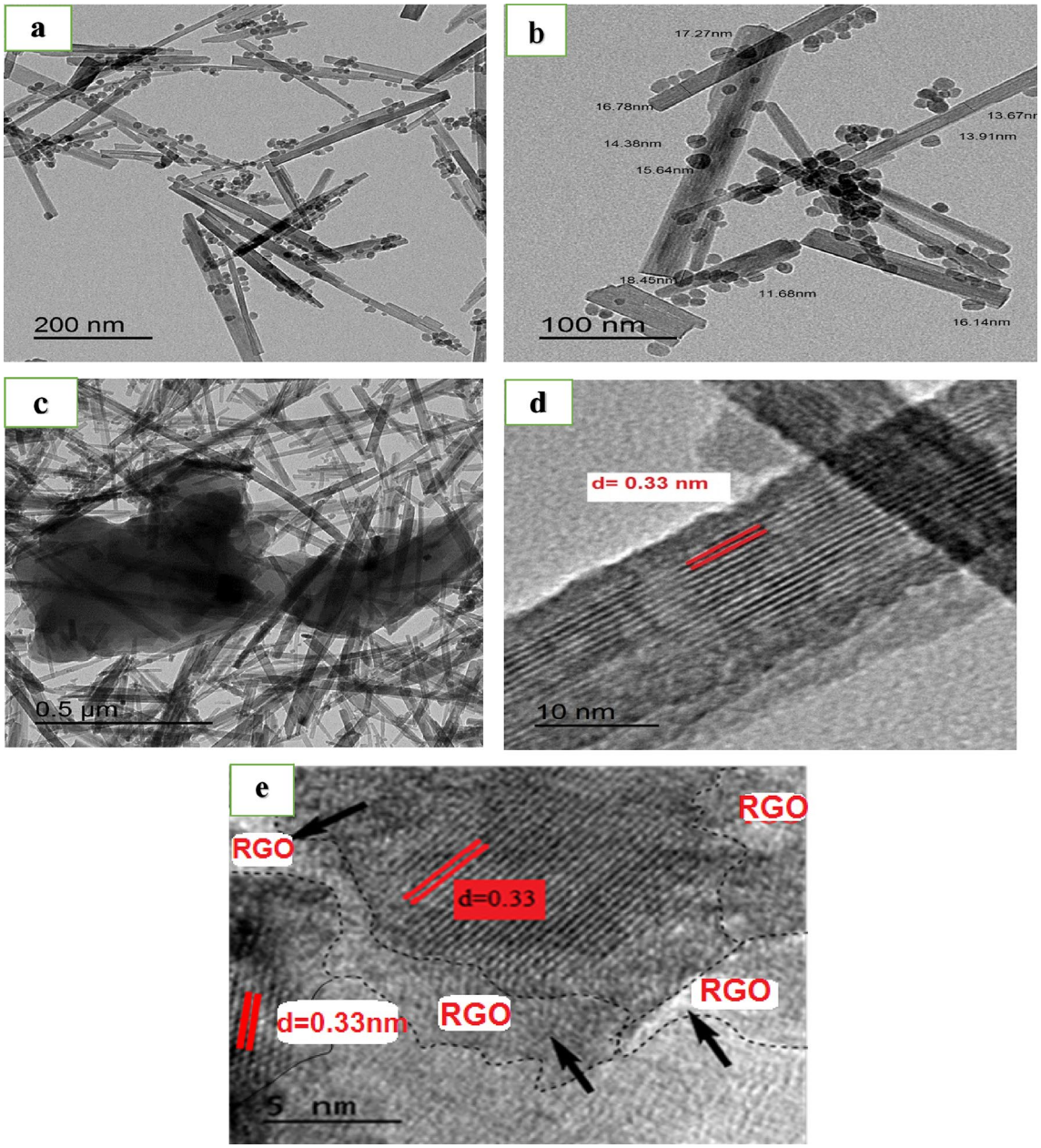

Figure 2. TEM and HR-TEM images of (**a**, **b**, **d**) Fe_3O_4–$FeVO_4$ and (**c**, **e**) 10%RGO/Fe_3O_4–$FeVO_4$.

observed in the spectrum of 10%RGO/Fe_3O_4–$FeVO_4$ (Fig. 4c) comparing with Fe_3O_4–$FeVO_4$. Also, Fig. 4c displays that the peaks located at 516.66 and 523.65 eV were shifted to 516.13 and 521.47 eV, respectively indicating the presence V^{3+} resulted due to the reduction of V^{4+} to V^{3+} state[23,40]. The formation of V^{4+} and V^{3+} in the sample indicates to existence of oxygen vacancies (Vo) in their crystal structure[23].

Figure 4d illustrates the spectrum of O 1*s* of Fe_3O_4–$FeVO_4$ showed three peaks located at 529.92, 530.37 and 532.54 eV assign to the lattice O in Fe_3O_4–$FeVO_4$[23,41]. However, 10%RGO/Fe_3O_4–$FeVO_4$ exhibited new peaks located at 529.46 and 531.66 eV attributed to the oxygen and hydroxyl groups on the RGO[2,25,39]. Also, Fig. 4d shows that the binding energies peaks of O 1*s* in the 10%RGO/Fe_3O_4–$FeVO_4$ were shifted to 529.97, 530.47 and 532.84 eV, indicating the existence of high Vo formed after the addition of RGO[17]. Figure 2S gives compression between GO and RGO. In the XPS spectrum of GO (Fig. 2S), four peaks appear at 284.59, 286.28, 288.33 and 289.06 eV are attributed to sp^2 and sp^3 carbon[20,42,43]. However, positional shift of the peaks located at 288.33 and 289.06 eV to 287.84 and 288.91 eV in the 10%RGO/Fe_3O_4–$FeVO_4$ were observed and the intensity of peaks that attributed to oxygenated groups were decreased sharply which indicates the effective reduction of GO to RGO[20,44]. Based on the results above the shifting in the peaks position of Fe 2*p*, V 2*p* and O1*s* in the 10%RGO/Fe_3O_4–$FeVO_4$ attribute to the strong interactions between Fe_3O_4–$FeVO_4$ and RGO in the nanocomposites[2,23].

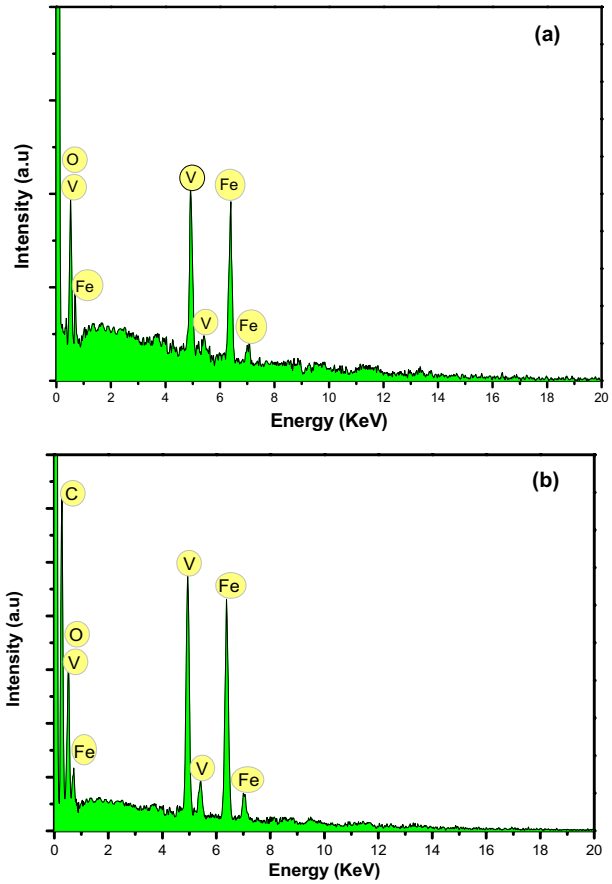

Figure 3. EDX spectra of (**a**) Fe_3O_4–$FeVO_4$ and (**b**) 10%RGO/Fe_3O_4–$FeVO_4$ nanocomposite.

DRS analyst. DRS spectra of Fe_3O_4–$FeVO_4$ and xRGO/Fe_3O_4–$FeVO_4$ with different RGO contents are depicted in Fig. 5. As depicted in Fig. 5, the samples showed strong absorption in the visible region. The absorbance threshold of Fe_3O_4–$FeVO_4$ appeared nearly at 705 nm. However, the absorption in the visible region (strong red-shift) improved largely in the xRGO/Fe_3O_4–$FeVO_4$ comparing with Fe_3O_4–$FeVO_4$ indicating improving the optical properties Fe_3O_4–$FeVO_4$ when composed with RGO[45]. The band gap energy (E_g) was calculated using Tauc's equation:

$$\alpha h\nu = A\left(h\nu - E_g\right)^n$$

where υ is the wavenumber, h is Planck constant, α is absorption coefficient, E_g is the energy band gap and A is a constant[9,29]. From the plot of $(\alpha h\upsilon)^{1/2}$ versus photon energy (eV) as shown in Fig. 3S, the band gap energies (E_g) of the prepared samples were calculated and the resulted values are listed in Table 1. As shown in Table 1, the band gap energy of Fe_3O_4–$FeVO_4$ is 2.06 eV whereas the E_g of xRGO/Fe_3O_4–$FeVO_4$ were narrowed from 2.04 of sample with 5%wt.% of RGO to 1.97 of sample with 15wt.% of RGO. The reducing in the E_g of xRGO/Fe_3O_4–$FeVO_4$ can attribute to the effect and overlap of different factors. New orbitals can formed in the xRGO/Fe_3O_4–$FeVO_4$ due to the electronic interactions between RGO and Fe_3O_4–$FeVO_4$ leading narrowing in the E_g of xRGO/Fe_3O_4–$FeVO_4$[25,46]. Another reason attributes to increase the Vo in the nanocomposite after the addition of RGO which contributes in the narrowing of E_g of Fe_3O_4–$FeVO_4$ due to creation of intermediated states of energy levels in the E_g of xRGO/Fe_3O_4–$FeVO_4$ causing narrowing in the E_g[47–49].

The creation of intermediated energy states and new molecular orbitals in the xRGO/Fe_3O_4–$FeVO_4$ improved the absorption in the visible region and also contributed in retarding the recombination of photocarriers charges leading improving the photoactivity of xRGO/Fe_3O_4–$FeVO_4$ under solar light[46].

PL spectra. The photoluminescence spectra (PL) of Fe_3O_4–$FeVO_4$ and xRGO/Fe_3O_4–$FeVO_4$ are displayed in Fig. 6. All the samples displayed similar PL spectra. Figure 6 illustrates that the emission peaks intensities of xRGO/Fe_3O_4–$FeVO_4$ decreased noticeably compared to the Fe_3O_4–$FeVO_4$, denoting the retardation of charges carriers (e–h) recombination after the addition of RGO. On the other hand, Fig. 6 showed that the 10%RGO/Fe_3O_4–$FeVO_4$ has the lowest intensity indicating the sample with 10 wt.% of RGO separated the photogenerated carriers effectively. The enhancing in the suppression of photocarriers of xRGO/Fe_3O_4–$FeVO_4$ resulted from the role of RGO which acted as efficient electrons trapping by creating of new defects or vacancies within the Fe_3O_4–$FeVO_4$ leading to enhancing the lifetime of photocarriers[50]. However, increasing the RGO amount

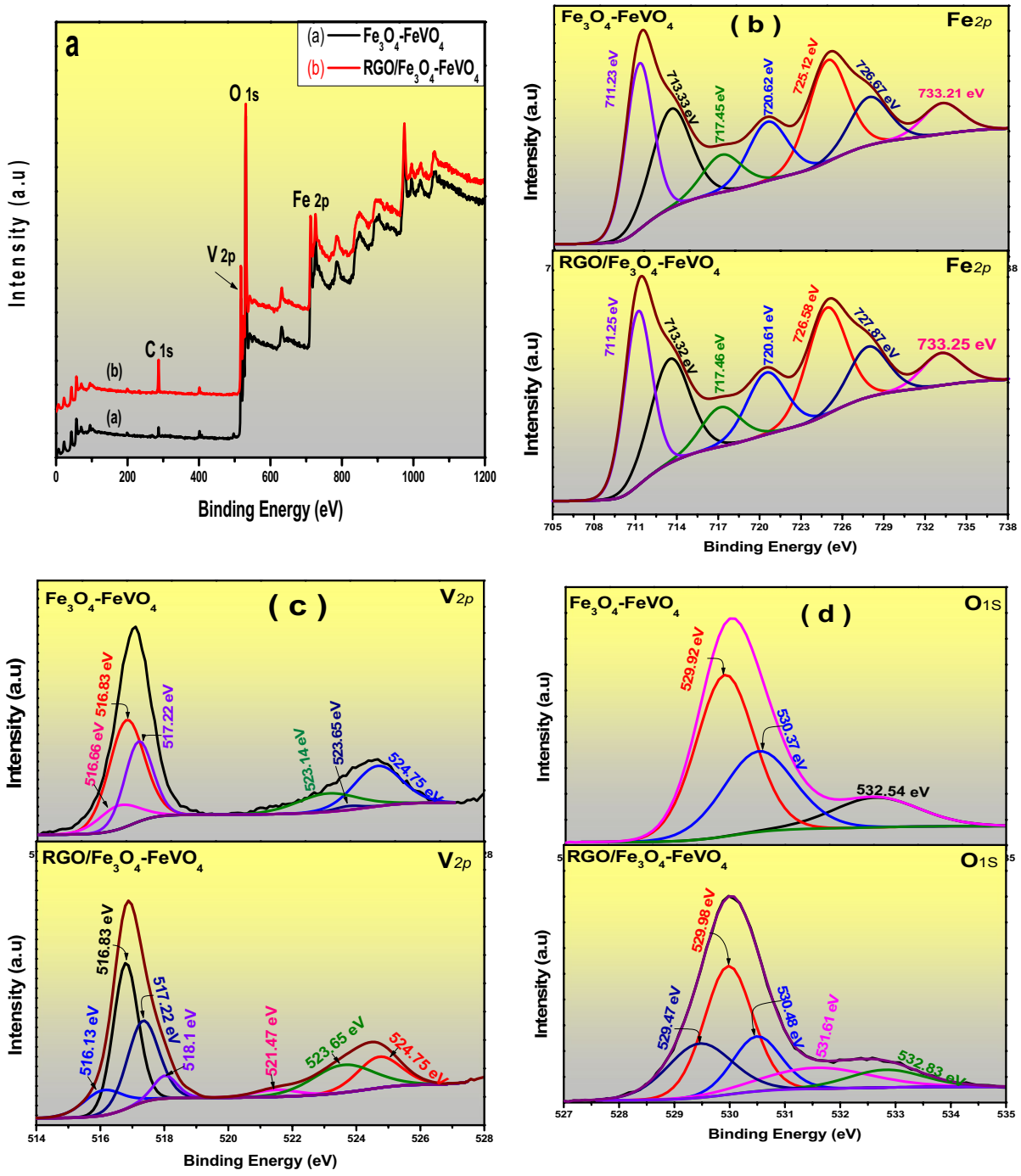

Figure 4. XPS spectra of Fe_3O_4–$FeVO_4$ and 10%RGO/Fe_3O_4–$FeVO_4$ nanocomposites.

beyond 10 wt.% accompanied by increasing the PL emission intensity (Fig. 6) indicating the opposite role of RGO where played as recombination centers and consequently accelerated the recombination rate of charges in the xRGO/Fe_3O_4–$FeVO_4$[20,28,46].

Photocurrent analysis. The transient photocurrent response of the prepared samples was determined under visible light[51]. Figure 4S exhibits stable and reversible photocurrent densities of the prepared catalysts after several runs of on and off. Also, Fig. 4S displays that the 10%RGO/Fe_3O_4–$FeVO_4$ showed the highest density comparing to other samples. Based on these results, the photocurrent density of the prepared catalysts strongly depends on the RGO content. These observations confirm the role of RGO in retardation the recombination and improving the transfer of photogenerated charges[52]. However, a reduction in the photocurrent response was observed after increasing the content of RGO to 15 wt.% indicating the opposite role of RGO as described above which in turn reduce the density of photocurrent.

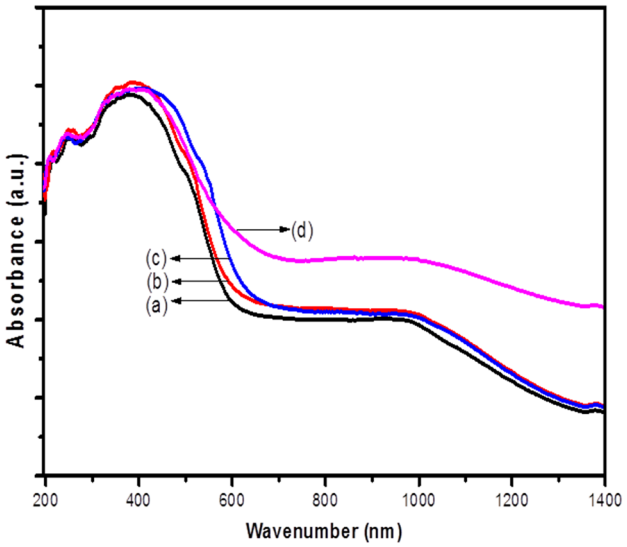

Figure 5. UV–Vis absorbance spectra of (**a**) Fe_3O_4–$FeVO_4$ and xRGO/Fe_3O_4–$FeVO_4$ at (**b**) 5%, (**c**) 10%, (**d**) 15% wt.% of RGO.

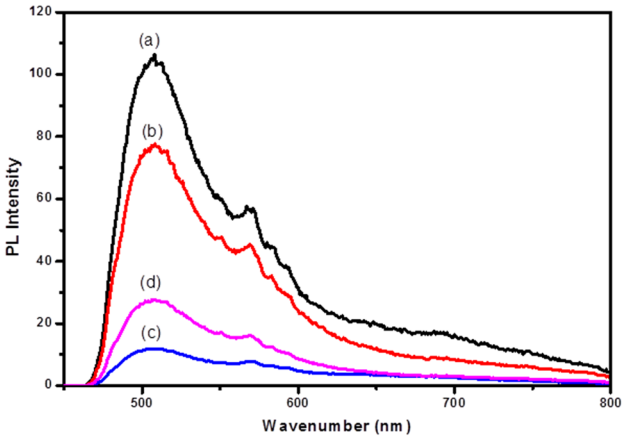

Figure 6. PL spectra of (**a**) Fe_3O_4–$FeVO_4$ and xRGO/Fe_3O_4–$FeVO_4$ at (**b**) 5%, (**c**) 10%, (**d**) 15% wt.% of RGO.

Photocatalytic performance. *Photodegradation studies.* The photocatalytic performances of the prepared samples were evaluated by the photodegradation of MB, phenol and BG under sunlight irradiation as displayed in Fig. 7 and Fig. 5S, respectively. No photoreaction was observed in absence the catalyst or light source. Comparing with Fe_3O_4–$FeVO_4$, the xRGO/Fe_3O_4–$FeVO_4$ showed the highest photocatalytic activity against of MB, phenol and BG. Also, the sample with 10 wt.% of RGO displayed the highest photoactivity compared with other samples. These results indicate that the addition of RGO enhanced the photocatalytic activity of Fe_3O_4–$FeVO_4$ by enhancing the suppression of the photogenerated charges recombination which in turn improved the photoactivity of Fe_3O_4–$FeVO_4$ under sunlight irradiation[46].

The total effect of RGO in improving and reducing the photoactivity of Fe_3O_4–$FeVO_4$ can attributed to the following reasons: the improving resulted due to the effect of RGO in acceleration the transition of electrons to the catalyst surface leading inhibition of the photogeneration charges recombination[20]. Also, the addition of RGO facilitated the transition of electrons from VB to CB due to creation of new levels of energy through the E_g of Fe_3O_4–$FeVO_4$ which in turn reduced the required energy for this transfer[53]. On the other hand, the reduction in the photoactivity of Fe_3O_4–$FeVO_4$ in the existence of high amount of RGO resulted from the shielding effect of RGO which restrained the absorption of incident photons to arrival at the active sites on the surface of Fe_3O_4–$FeVO_4$[20]. Moreover, increasing the amount of RGO acted as recombination centers of electrons and holes pairs[20,28,46].

According to the Langmuir–Hinshelwood kinetics model, the photodegradation process of MB, phenol and BG over Fe_3O_4–$FeVO_4$ and xRGO/Fe_3O_4–$FeVO_4$ using the following formula[28]:

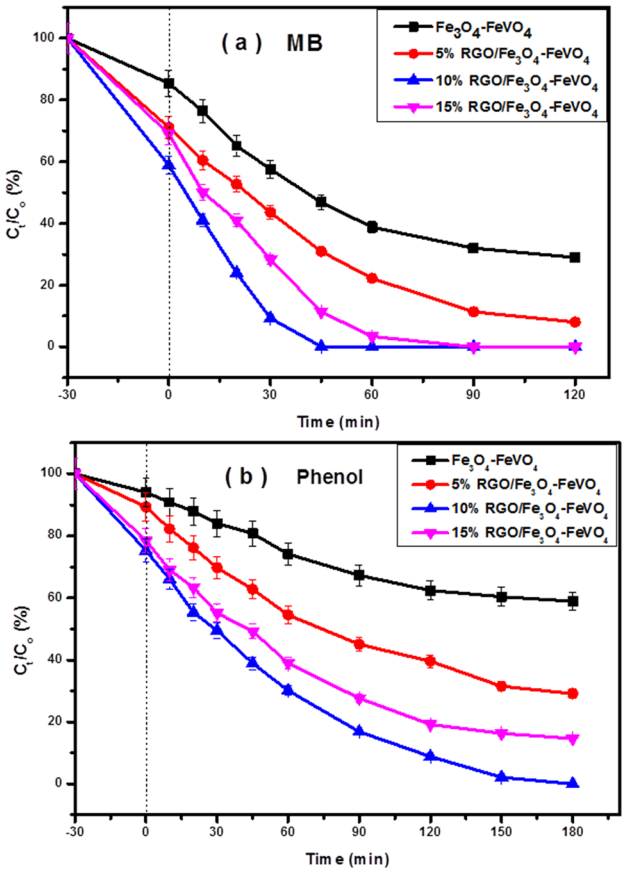

Figure 7. Photocatalytic degradation of (**a**) MB and (**b**) phenol over of Fe_3O_4–$FeVO_4$ and xRGO/Fe_3O_4–$FeVO_4$ nanocomposites versus irradiation time with error bars.

$$\ln\left(\frac{C_o}{C_t}\right) = kt$$

where k is the photodegradation rate constant, C_o and C are the original concentration and concentration of pollutant at time t. The linear approximation of the kinetics equation is shown in Fig. 6S. The apparent values of k and correlation coefficient (R^2) were calculated and listed in Table 2. The values of R^2 indicated that the degradation of MB, phenol and BG follows pseudo 1st order kinetics. Also, Table 2 shows the values of k increased with increasing the RGO content and the sample with 10 wt.% of RGO displayed the highest photodegradation rate compared with other tested photocatalysts.

Figure 7S illustrates the values of %TOC of MB, phenol and BG degradation over 10%RGO/Fe_3O_4–$FeVO_4$. The results illustrated that the mineralization of MB, phenol and BG after 180 min was 92.8%, 85.3% and 99.9%, respectively. Comparing these results with the photodegradation results we found the values of %TOC were lower than the photodegradation values. This indicates to existence of some un-degraded intermediates (colorless). However, with increasing the irradiation time to 360 min, the %TOC values increased sharply to achieve 100% of mineralization of both MB, phenol and BG.

Table 1S displays comparison between the photocatalytic activity of our samples that obtained in this work and that found in other literatures[17,19,20,22,23,25,27,54–58]. As shown in Table 1S the 10%RGO/Fe_3O_4–$FeVO_4$ showed the highest photoactivity for photodegradation of organic pollutants under solar light. Also, our samples showed high visible light absorption, photogenerated charges separation and reusability. Moreover, in this work, the reduction of graphene oxide was performed effectively without using chemical reduction agents by green reduction method and during short time (2 h) comparing to other literatures.

Photocatalytic mechanism. To understand the photodegradation mechanism of MB, the radical scavengers were added during the photodegradation of MB. Figure 8S shows effect the addition of scavengers on the degradation of MB over 10%RGO/Fe_3O_4–$FeVO_4$ sample. As shown in Fig. 8S, the addition of BQ ($\cdot O_2^-$ radical) was accompanied with sharply reduction in the degradation of MB while the addition of Na_2EDTA (h^+ radical) and IPA ($\cdot OH$ radical) accompanied with high suppression for Na_2EDTA and venial reduction for IPA. These results imply that the $\cdot O_2^-$ played the main role in degradation of MB while the $\cdot OH$ played the minor role. This indicates that the $\cdot O_2^-$ is the more active radical contributed in the degradation of MB.

Samples	MB		Phenol		BG	
	K_1	R^2	K_1	R^2	K_1	R^2
Fe_3O_4–$FeVO_4$	0.01428	0.99766	0.00592	0.99318	0.01122	0.98814
5%RGO/Fe_3O_4–$FeVO_4$	0.02304	0.99862	0.01061	0.99643	0.01749	0.99626
10%RGO/Fe_3O_4–$FeVO_4$	0.0601	0.99959	0.02257	0.02257	0.04989	0.99846
15%RGO/Fe_3O_4–$FeVO_4$	0.04161	0.9986	0.01599	0.01599	0.03295	0.99875

Table 2. Correlation coefficients and rate constants for MB, phenol and BG photodegradation.

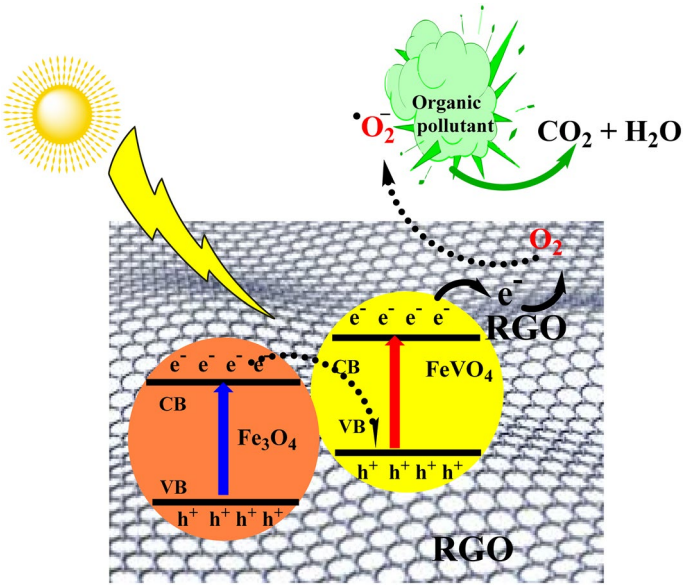

Figure 8. Postulated mechanism of electron transfer in xRGO/Fe_3O_4–$FeVO_4$ nanocomposites.

From the radical scavengers results, the possible mechanism of the degradation of MB, phenol and BG over xRGO/Fe_3O_4–$FeVO_4$ was suggested as a direct Z-scheme as proposed in Fig. 8. In this mechanism, when the xRGO/Fe_3O_4–$FeVO_4$ absorbed the sunlight illumination, the incident photons promoted transfer of electrons (e^-) to the CB of $FeVO_4$ and the holes (h^+) accumulated in the VB of Fe_3O_4 [Eqs. (3), (4)]. The photoinduced e^- on the CB of Fe_3O_4 can transfer to the VB of $FeVO_4$, and then quickly recombine with the h^+ of $FeVO_4$ were achieved, which is favorable for higher separation rate of e^--h^+ pairs of the single photocatalyst and higher redox potential[59,60]. In this case, the e^- accumulated in CB of $FeVO_4$ are taken by the RGO and then reduce O_2 into $^{\cdot}O^{2-}$ [Eqs. (5), (6)], while the h^+ in VB of Fe_3O_4 VB are more positive potential and has sufficient oxidation capacity to oxidize OH^- into $^{\cdot}OH$ or react with pollutants molecules directly [Eqs. (7–9)][59–63]. These results imply the contribution of generated radicals in the degradation of MB and phenol to gives CO_2 and H_2O.

$$Fe_3O_4 + h\nu(\text{photon}) \rightarrow e^- + Fe_3O_4^*(h^+) \tag{3}$$

$$FeVO_4 + e^- \rightarrow FeVO_4(e^-) \tag{4}$$

$$FeVO_4(e^-) + RGO \rightarrow RGO(e^-) \tag{5}$$

$$RGO(e^-) + O_2 \rightarrow RGO + {}^{\cdot}O_2^- \tag{6}$$

$$Fe_3O_4^*(h^+) + H_2O \rightarrow H^+ + OH^- \tag{7}$$

$$Fe_3O_4^*(h^+) + OH^- \rightarrow {}^{\cdot}OH \tag{8}$$

$${}^{\cdot}O_2^- + h_{VB}^+ + {}^{\cdot}OH + \text{Organic pollutants} \rightarrow CO_2 + H_2O \tag{9}$$

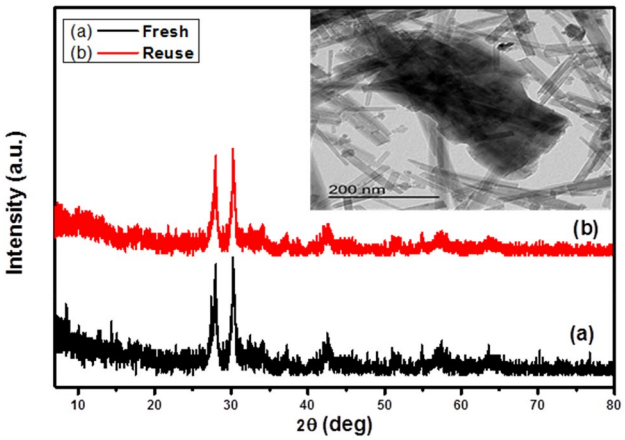

Figure 9. Effect of reuse on the structural properties of 10% rGO/$FeVO_4$ nanocomposites.

Reusability study. The reusability and stability of 10%RGO/Fe_3O_4–$FeVO_4$ were studied. Figure 9S displays the degradation of MB, phenol and BG after four cycles (runs) under the same conditions. The catalyst powder was separated from the reaction mixture after each run and soaked in ethanol for 1 h. Then, the powder was washed with water and finally dried at 100 °C for 8 h[30]. The obtain results illustrated no significant decline in photodegradation activity of 10%RGO/Fe_3O_4–$FeVO_4$ was observed after five runs. To investigate the effect of reused times on the structural properties of catalyst, the 10%RGO/Fe_3O_4–$FeVO_4$ was investigated by the XRD and TEM techniques before and after reuse as shown in Fig. 9 and the results showed no changes were observed in the structural properties of 10%RGO/Fe_3O_4–$FeVO_4$ indicating the excellent reusability and sustainability of the prepared photocatalysts.

Conclusion

Fe_3O_4–$FeVO_4$ and xRGO/Fe_3O_4–$FeVO_4$ were successfully prepared by the hydrothermal method. The results confirmed successfully reduction GO to RGO by green method. The UV–Vis results showed improving of the absorption in the visible region and enhancing of the photogenerated charges separation of after the addition of RGO. The samples showed excellent degradation of MB, phenol, BG after the addition of RGO under sunlight illumination and the sample with 10 wt.% of RGO exhibited the highest photodegradation efficiency. The TOC analysis illustrated that the MB and phenol completely mineralized after 360 min. The results of scavenger tests showed that the $^{\cdot}O_2^-$ played the main role in oxidant of MB. The kinetic studies results illustrated that the degradation of MB and phenol follows the pseudo 1st order kinetics. The prepared samples showed excellent reusability after five runs without significant reduction in the photoaactivity. Based on these results, we can be concluded that the xRGO/Fe_3O_4–$FeVO_4$ are suitable and convenient material for treatment of organic pollutants and industrial effluent.

Received: 3 January 2022; Accepted: 7 April 2022
Published online: 21 April 2022

References

1. Biswas, S. K. & Baeg, J. O. Enhanced photoactivity of visible light responsive W incorporated $FeVO_4$ photoanode for solar water splitting. *Int. J. Hydrog. Energy* **38**, 14451–14457. https://doi.org/10.1016/j.ijhydene.2013.09.064 (2013).
2. Long, X. *et al.* Bamboo shoots shaped $FeVO_4$ passivated ZnO nanorods photoanode for improved charge separation/transfer process towards efficient solar water splitting. *Appl. Catal. B Environ.* **257**, 117813. https://doi.org/10.1016/j.apcatb.2019.117813 (2019).
3. Jansi Rani, B. *et al.* Ni supported anorthic phase $FeVO_4$ nanorods for electrochemical water oxidation. *Mater. Lett.* **275**, 128091. https://doi.org/10.1016/j.matlet.2020.128091 (2020).
4. Appavu, B., Thiripuranthagan, S., Ranganathan, S., Erusappan, E. & Kannan, K. $BiVO_4$/N-rGO nano composites as highly efficient visible active photocatalyst for the degradation of dyes and antibiotics in eco system. *Ecotoxicol. Environ. Saf.* **151**, 118–126. https://doi.org/10.1016/j.ecoenv.2018.01.008 (2018).
5. Hassan, S. M. & Mannaa, M. A. Photocatalytic degradation of brilliant green dye by SnO_2/TiO_2 nanocatalysts. *Int. J. Nano Mater. Sci.* **5**, 9–19 (2016).
6. Mannaa, M. A., Altass, H. M. & Salama, R. S. MCM-41 grafted with citric acid: The role of carboxylic groups in enhancing the synthesis of xanthenes and removal of heavy metal ions. *Environ. Nanotechnol. Monit. Manag.* **15**, 100410. https://doi.org/10.1016/j.enmm.2020.100410 (2021).
7. Sajid, M. M. *et al.* Morphological effects on the photocatalytic performance of $FeVO_4$ nanocomposite. *Nano-Struct. Nano-Objects* **22**, 100431. https://doi.org/10.1016/j.nanoso.2020.100431 (2020).
8. Mannaa, M. A., Qasim, K. F., Alshorifi, F. T., El-Bahy, S. M. & Salama, R. S. Role of NiO nanoparticles in enhancing structure properties of TiO_2 and its applications in photodegradation and hydrogen evolution. *ACS Omega* **6**, 30386–30400. https://doi.org/10.1021/acsomega.1c03693 (2021).
9. Alshorifi, F. T. *et al.* Facile and green synthesis of silver quantum dots immobilized onto a polymeric CTS-PEO blend for the photocatalytic degradation of p-nitrophenol. *ACS Omega* **6**, 30432–30441. https://doi.org/10.1021/acsomega.1c03735 (2021).

10. Altass, H. M. *et al.* Enhanced catalytic activity for CO oxidation by highly active Pd nanoparticles supported on reduced graphene oxide/copper metal organic framework. *J. Taiwan Inst. Chem. Eng.* **128**, 194–208. https://doi.org/10.1016/j.jtice.2021.08.034 (2021).
11. Bantawal, H., Shenoy, U. S. & Bhat, D. K. Vanadium doped $CaTiO_3$ cuboids: Role of vanadium in improving the photocatalytic activity. *Nanoscale Adv.* **3**, 5301–5311. https://doi.org/10.1039/d1na00468a (2021).
12. Shenoy, U. S., Bantawal, H. & Bhat, D. K. Band Engineering of $SrTiO_3$: Effect of synthetic technique and site occupancy of doped rhodium. *J. Phys. Chem. C* **122**, 27567–27574. https://doi.org/10.1021/acs.jpcc.8b10083 (2018).
13. Bhat, D. K., Bantawal, H. & Shenoy, U. S. Rhodium doping augments photocatalytic activity of barium titanate: Effect of electronic structure engineering. *Nanoscale Adv.* **2**, 5688–5698. https://doi.org/10.1039/d0na00702a (2020).
14. Bantawal, H., Sethi, M., Shenoy, U. S. & Bhat, D. K. Porous Graphene Wrapped $SrTiO_3$ nanocomposite: Sr-C bond as an effective coadjutant for high performance photocatalytic degradation of methylene blue. *ACS Appl. Nano Mater.* **2**, 6629–6636. https://doi.org/10.1021/acsanm.9b01513 (2019).
15. Mishra, A. *et al.* Comparative electrochemical analysis of rGO-$FeVO_4$ nanocomposite and $FeVO_4$ for supercapacitor application. *Appl. Surf. Sci.* **488**, 221–227. https://doi.org/10.1016/j.apsusc.2019.05.259 (2019).
16. Zhang, M. *et al.* Elucidation of the opto-electronic and photoelectrochemical properties of $FeVO_4$ photoanodes for solar water oxidation. *J. Mater. Chem. A* **6**, 548–555. https://doi.org/10.1039/c7ta08923f (2018).
17. Li, N. *et al.* Facile preparation of $BiVO_4$/$FeVO_4$ heterostructure for efficient water-splitting applications. *Int. J. Hydrog. Energy* **44**, 23046–23053. https://doi.org/10.1016/j.ijhydene.2019.07.063 (2019).
18. Zhang, L., Cao, X. F., Ma, Y. L., Chen, X. T. & Xue, Z. L. Microwave-assisted solution-phase preparation and growth mechanism of $FeMoO_4$ hierarchical hollow spheres. *CrystEngComm* **12**, 207–210. https://doi.org/10.1039/b912555h (2010).
19. Dutta, D. P., Ramakrishnan, M., Roy, M. & Kumar, A. Effect of transition metal doping on the photocatalytic properties of $FeVO_4$ nanoparticles. *J. Photochem. Photobiol. A Chem.* **335**, 102–111. https://doi.org/10.1016/j.jphotochem.2016.11.022 (2017).
20. Yang, R. *et al.* One-step preparation (3D/2D/2D) $BiVO_4$/$FeVO_4$@rGO heterojunction composite photocatalyst for the removal of tetracycline and hexavalent chromium ions in water. *Chem. Eng. J.* **390**, 124522. https://doi.org/10.1016/j.cej.2020.124522 (2020).
21. Zhang, H. *et al.* The $FeVO_4{\cdot}0.9H_2O$/graphene composite as anode in aqueous magnesium ion battery. *Electrochim. Acta* **256**, 357–364. https://doi.org/10.1016/j.electacta.2017.10.038 (2017).
22. Rahimpour, R., Chaibakhsh, N., Zanjanchi, M. A. & Moradi-Shoeili, Z. Fabrication of ZnO/$FeVO_4$ heterojunction nanocomposite with high catalytic activity in photo-Fenton-like process. *J. Alloys Compd.* **817**, 152702. https://doi.org/10.1016/j.jallcom.2019.152702 (2020).
23. Chachvalvutikul, A., Jakmunee, J., Thongtem, S., Kittiwachana, S. & Kaowphong, S. Novel $FeVO_4$/$Bi_7O_9I_3$ nanocomposite with enhanced photocatalytic dye degradation and photoelectrochemical properties. *Appl. Surf. Sci.* **475**, 175–184. https://doi.org/10.1016/j.apsusc.2018.12.214 (2019).
24. Sadiq, M. M. J., Shenoy, U. S. & Bhat, D. K. Novel RGO-$ZnWO_4$-Fe_3O_4 nanocomposite as high performance visible light photocatalyst. *RSC Adv.* **6**, 61821–61829. https://doi.org/10.1039/c6ra13002j (2016).
25. Sadiq, M. M. J., Shenoy, U. S. & Bhat, D. K. Enhanced photocatalytic performance of N-doped RGO-$FeWO_4$/Fe_3O_4 ternary nanocomposite in environmental applications. *Mater. Today Chem.* **4**, 133–141. https://doi.org/10.1016/j.mtchem.2017.04.003 (2017).
26. Sadiq, M. M. J., Shenoy, U. S. & Bhat, D. K. Synthesis of $BaWO_4$/NRGO–g-C_3N_4 nanocomposites with excellent multifunctional catalytic performance via microwave approach. *Front. Mater. Sci.* **12**, 247–263. https://doi.org/10.1007/s11706-018-0433-0 (2018).
27. Alsulami, Q. A., Rajeh, A., Mannaa, M. A., Albukhari, S. M. & Baamer, D. F. Preparation of highly efficient sunlight driven photodegradation of some organic pollutants and H_2 evolution over rGO/$FeVO_4$ nanocomposites. *Int. J. Hydrog. Energy* **46**, 27349–27363. https://doi.org/10.1016/j.ijhydene.2021.05.211 (2021).
28. Hassan, S. M., Ahmed, A. I. & Mannaa, M. A. Structural, photocatalytic, biological and catalytic properties of SnO_2/TiO_2 nanoparticles. *Ceram. Int.* **44**, 6201–6211. https://doi.org/10.1016/j.ceramint.2018.01.005 (2018).
29. Hassan, S. M., Ahmed, A. I. & Mannaa, M. A. Preparation and characterization of SnO_2 doped TiO_2 nanoparticles: Effect of phase changes on the photocatalytic and catalytic activity. *J. Sci. Adv. Mater. Devices* **4**, 400–412. https://doi.org/10.1016/j.jsamd.2019.06.004 (2019).
30. Hassan, S. M., Ahmed, A. I. & Mannaa, M. A. Surface acidity, catalytic and photocatalytic activities of new type $H_3PW_{12}O_{40}$/Sn-TiO_2 nanoparticles. *Colloids Surf. A Physicochem. Eng. Asp.* **577**, 147–157. https://doi.org/10.1016/j.colsurfa.2019.05.070 (2019).
31. Khan, M. *et al.* Functionalized nano diamond composites for photocatalytic hydrogen evolution and effective pollutant degradation. *Int. J. Hydrog. Energy* **45**, 29070–29081. https://doi.org/10.1016/j.ijhydene.2020.07.274 (2020).
32. Zhang, J., Zhao, W., Li, Z., Lu, G. & Zhu, M. Visible-light-assisted peroxymonosulfate activation over Fe(II)/V(IV) self-doped $FeVO_4$ nanobelts with enhanced sulfamethoxazole degradation: Performance and mechanism. *Chem. Eng. J.* **403**, 126384. https://doi.org/10.1016/j.cej.2020.126384 (2021).
33. Li, J. *et al.* Facile synthesis and high activity of novel $BiVO_4$ /$FeVO_4$ heterojunction photocatalyst for degradation of metronidazole. *Appl. Surf. Sci.* **351**, 270–279. https://doi.org/10.1016/j.apsusc.2015.05.134 (2015).
34. Zolfagharinia, S., Kolvari, E., Koukabi, N. & Hosseini, M. M. Core-shell zirconia-coated magnetic nanoparticles offering a strong option to prepare a novel and magnetized heteropolyacid based heterogeneous nanocatalyst for three- and four-component reactions. *Arab. J. Chem.* **13**, 227–241. https://doi.org/10.1016/j.arabjc.2017.04.004 (2020).
35. Hashtroudi, H. *et al.* Hydrogen gas sensing properties of microwave-assisted 2D Hybrid Pd/rGO: Effect of temperature, humidity and UV illumination. *Int. J. Hydrog. Energy* **46**, 7653–7665. https://doi.org/10.1016/j.ijhydene.2020.11.268 (2021).
36. Hassan, S. M. H., Mannaa, M. A. & Ibrahim, A. A. Nano-sized mesoporous phosphated tin oxide as an efficient solid acid catalyst. *RSC Adv.* **9**, 810–818. https://doi.org/10.1039/C8RA08962K (2019).
37. Ibrahim, A. A., Hassan, S. M. & Mannaa, M. A. Mesoporous tin oxide-supported phosphomolybdic acid as high performance acid catalysts for the synthesis of hydroquinone diacetate. *Colloids Surf. A Physicochem. Eng. Asp.* **586**, 124248. https://doi.org/10.1016/j.colsurfa.2019.124248 (2020).
38. Meng, L. *et al.* Enhanced electrochemical performance of a promising anode material $FeVO_4$ by tungsten doping. *Ceram. Int.* **46**, 21360–21366. https://doi.org/10.1016/j.ceramint.2020.05.232 (2020).
39. Niu, X. *et al.* Amorphous $FeVO_4$ as a promising anode material for potassium-ion batteries. *Energy Storage Mater.* **22**, 160–167. https://doi.org/10.1016/j.ensm.2019.01.011 (2019).
40. Lan, B. *et al.* $FeVO_4{\cdot}nH_2O$@rGO nanocomposite as high performance cathode materials for aqueous Zn-ion batteries. *J. Alloys Compd.* **818**, 153372. https://doi.org/10.1016/j.jallcom.2019.153372 (2020).
41. Yu, Y. *et al.* Peroxidase-like activity of $FeVO_4$ nanobelts and its analytical application for optical detection of hydrogen peroxide. *Sens. Actuators B Chem.* **233**, 162–172. https://doi.org/10.1016/j.snb.2016.04.041 (2016).
42. Wang, T. *et al.* Reduced graphene oxide (rGO)/$BiVO_4$ composites with maximized interfacial coupling for visible lght photocatalysis. *ACS Sustain. Chem. Eng.* **2**, 2253–2258. https://doi.org/10.1021/sc5004665 (2014).
43. Yang, Z., He, R., Wu, H., Ding, Y. & Mei, H. Needle-like CoP/rGO growth on nickel foam as an efficient electrocatalyst for hydrogen evolution reaction. *Int. J. Hydrog. Energy* **46**, 9690–9698. https://doi.org/10.1016/j.ijhydene.2020.07.114 (2021).
44. Zhang, L. *et al.* Synthesis of butterfly-like $BiVO_4$/RGO nanocomposites and their photocatalytic activities. *Chin. J. Chem. Eng.* **26**, 667–674. https://doi.org/10.1016/j.cjche.2017.09.007 (2018).
45. He, G. L. *et al.* Hydrothermal synthesis of $FeWO_4$ -graphene composites and their photocatalytic activities under visible light. *Appl. Surf. Sci.* **351**, 474–479. https://doi.org/10.1016/j.apsusc.2015.05.159 (2015).

46. Fang, D. *et al.* $BiVO_4$-rGO with a novel structure on steel fabric used as high-performance photocatalysts. *Sci. Rep.* **7**, 1–9. https://doi.org/10.1038/s41598-017-07342-1 (2017).
47. Eshaq, G., Wang, S., Sun, H. & Sillanpaa, M. Superior performance of $FeVO_4$@CeO_2 uniform core-shell nanostructures in heterogeneous Fenton-sonophotocatalytic degradation of 4-nitrophenol. *J. Hazard. Mater.* **382**, 121059. https://doi.org/10.1016/j.jhazmat.2019.121059 (2020).
48. Vinoth, R., Karthik, P., Muthamizhchelvan, C., Neppolian, B. & Ashokkumar, M. Carrier separation and charge transport characteristics of reduced graphene oxide supported visible-light active photocatalysts. *Phys. Chem. Chem. Phys.* **18**, 5179–5191. https://doi.org/10.1039/c5cp08041j (2016).
49. Ren, X. *et al.* Band gap engineering of BiOI: Via oxygen vacancies induced by graphene for improved photocatalysis. *New J. Chem.* **43**, 1523–1530. https://doi.org/10.1039/c8nj05538f (2019).
50. Sajid, M. M. *et al.* Fast surface charge transfer with reduced band gap energy of $FeVO_4$/graphene nanocomposite and study of its electrochemical property and enhanced photocatalytic activity. *Arab. J. Sci. Eng.* **44**, 6659–6667. https://doi.org/10.1007/s13369-019-03927-2 (2019).
51. Peng, W., Zhang, S. S., Shao, Y. B. & Huang, J. H. Bimetallic PtNi/g-C_3N_4 nanotubes with enhanced photocatalytic activity for H_2 evolution under visible light irradiation. *Int. J. Hydrog. Energy* **43**, 22215–22225. https://doi.org/10.1016/j.ijhydene.2018.10.102 (2018).
52. Chen, K. L. *et al.* Excellent visible light photocatalytic efficiency of Na and S co-doped g-C_3N_4 nanotubes for H2 production and organic pollutant degradation. *Int. J. Hydrog. Energy* **44**, 31916–31929. https://doi.org/10.1016/j.ijhydene.2019.10.060 (2019).
53. Bashir, A. *et al.* Influence of nickel and lanthanum ions co-doping on photocatalytic properties of TiO_2 for effective degradation of reactive yellow 145 in the visible region. *J. Sol-Gel Sci. Technol.* **93**, 438–451. https://doi.org/10.1007/s10971-019-05162-5 (2020).
54. Bera, G. *et al.* Methylene blue dye degradation by bulk, nano $FeVO_4$ and rGO-$FeVO_4$. *3rd Int. Conf. Condens. Matter Appl. Phys.* **2220**, 80070. https://doi.org/10.1063/5.0001217 (2020).
55. Mohamed, M. J. S., Shenoy, S. & Bhat, D. K. Novel NRGO-$CoWO_4$-Fe_2O_3 nanocomposite as an efficient catalyst for dye degradation and reduction of 4-nitrophenol. *Mater. Chem. Phys.* **208**, 112–122. https://doi.org/10.1016/j.matchemphys.2018.01.012 (2018).
56. B. Appavu, S. Thiripuranthagan, S. Ranganathan, E. Erusappan, K. Kannan, $BiVO_4$ /N-rGO nano composites as highly efficient visible active photocatalyst for the degradation of dyes and antibiotics in eco system, in: Ecotoxicol. Environ. Saf., Elsevier Inc., 2018: pp. 118–126. https://doi.org/10.1016/j.ecoenv.2018.01.008.
57. Chen, H. *et al.* Improved visible light photocatalytic activity of mesoporous $FeVO_4$ nanorods synthesized using a reactable ionic liquid. *Cuihua Xuebao/Chin. J. Catal.* **40**, 744–754. https://doi.org/10.1016/s1872-2067(19)63272-9 (2019).
58. Liu, X. & Kang, Y. Synthesis and high visible-light activity of novel Bi_2O_3/$FeVO_4$ heterojunction photocatalyst. *Mater. Lett.* **164**, 229–231. https://doi.org/10.1016/j.matlet.2015.10.137 (2016).
59. Wang, Q., Liu, Z., Lu, Q., Guo, E. & Wei, M. Fabrication of direct Z-scheme α-Fe_2O_3/$FeVO_4$ nanobelts with enhanced photoelectrochemical performance. *ChemistrySelect* **3**, 809–815. https://doi.org/10.1002/slct.201702654 (2018).
60. Xu, G., Du, M., Li, T., Guan, Y. & Guo, C. Facile synthesis of magnetically retrievable Fe_3O_4/$BiVO_4$/CdS heterojunction composite for enhanced photocatalytic degradation of tetracycline under visible light. *Sep. Purif. Technol.* **275**, 119157. https://doi.org/10.1016/j.seppur.2021.119157 (2021).
61. Dehghan, S., Jafari, A. J., FarzadKia, M., Esrafili, A. & Kalantary, R. R. Visible-light-driven photocatalytic degradation of Metalaxyl by reduced graphene oxide/Fe_3O_4/ZnO ternary nanohybrid: Influential factors, mechanism and toxicity bioassay. *J. Photochem. Photobiol. A Chem.* **375**, 280–292. https://doi.org/10.1016/j.jphotochem.2019.01.024 (2019).
62. Yan, X., Liu, K. & Shi, W. Facile synthesis of CdS/$MnWO_4$ heterojunction with enhanced visible-light-driven photocatalytic activity and mechanism investigation. *Colloids Surf. A Physicochem. Eng. Asp.* **520**, 138–145. https://doi.org/10.1016/j.colsurfa.2017.01.065 (2017).
63. Xie, T. *et al.* Magnetic photocatalyst $BIVO_4$/Mn-Zn ferrite/reduced graphene oxide: Synthesis strategy and its highly photocatalytic activity. *Nanomaterials* https://doi.org/10.3390/nano8060380 (2018).

Acknowledgements

The authors extend their appreciation to the Deputyship for Research and Innovation, Ministry of Education in Saudi Arabia for funding this research work through the Project Number IFPHI-027-247-2020. and King Abdulaziz University, DSR, Jeddah, Saudi Arabia.

Author contributions

All authors contributed in writing and analyzing data.

Competing interests

The authors declare no competing interests.

Additional information

Supplementary Information The online version contains supplementary material available at https://doi.org/10.1038/s41598-022-10542-z.

Correspondence and requests for materials should be addressed to Q.A.A.

Reprints and permissions information is available at www.nature.com/reprints.

Publisher's note Springer Nature remains neutral with regard to jurisdictional claims in published maps and institutional affiliations.